Chapter 6

Recovery of hybrid $Cu(OH)_2$/CuO and CuO nanostructures from strip solution of spent PCBs of mobile phones and evaluation of their photocatalytic activity

6. Recovery of hybrid $Cu(OH)_2$/CuO and CuO nanostructures from strip solution of spent PCBs of mobile phones and evaluation of their photocatalytic activity

6.1. Introduction

The monoclinic structure of CuO, a lower band gap semiconductor, renders it highly reactive and its significant surface area offers notable potential in catalytic applications (Ramesh, 2021). Photocatalysis utilizes a semiconductor catalyst capable of capturing sunlight photons and generating electron-hole pairs, which assist in breaking down organic dyes using a safe and eco-friendly approach (Dong et al., 2015). Utilizing catalysts that can effectively absorb visible light while also meeting various practical requirements such as versatility, affordability, recyclability, and ease of fabrication is crucial. With their narrow energy gaps, cuprous oxide (Cu_2O), cupric oxide (CuO), and copper hydroxide ($Cu(OH)_2$) emerge as promising contenders for these reasons (Meyer et al., 2012). Furthermore, photocatalysts comprising heterogenous structures that incorporate two or more copper compounds, such as Cu_xO@Cu (Al-Jawhari et al., 2019; Alhebshi et al., 2020; Sun, 2015) or Cu_xO-$Cu(OH)_2$ (Hu et al., 2020; Murugadoss et al., 2021), have demonstrated higher efficiency compared to pure copper oxides. This improved performance can be attributed to the creation of heterojunctions, which enhance the separation of electron-hole pairs generated during photocatalysis, thereby enhancing the overall photocatalytic activity (Mamba et al., 2017). Marathey et al. reported that hierarchical nanostructure and nano heterojunctions offer improved performance, such as enhanced charge storage, by facilitating thermodynamically favourable charge transport from multiple active components when compared to the single-phase material (Marathey et al., 2019). Hence heterojunction hybrid nanomaterials are of great importance in photocatalysis as well as energy storage materials.

The prime focus of this research is to produce a nanostructure from electronic waste and to study its application as a simple, cost-effective and efficient photocatalyst. In Chapter 4 we synthesized CuO NPs from the leach liquor of WPCBs of computer motherboards. In the current chapter we plan to synthesize hybrid nanostructures from Cu-rich strip solution of discarded mobile phone PCBs. The nanoproduct is subject to various characterization techniques to confirm its phase, morphology and bandgap energy. Its photocatalytic activity is further explored for disintegration of RhB dye under light source in the visible spectrum. This approach to recovery is both cost-efficient and ecologically responsible. The utilization of synthesized hybrid nanostructures for dye degradation presents an opportunity to investigate the circular economy approach for metal reclamation in WPCBs, where the recycling and reuse of materials are central principles.

6.2. Synthesis of hybrid $Cu(OH)_2$/CuO and CuO nanostructures from strip solution of mobile phone PCBs

In the present study, a sustainable CuO nanoparticle recovery process from the Cu-rich stripped solution of spent mobile phone PCBs is investigated. $Cu(OH)_2$/CuO and CuO nanostructures are synthesized by a combination of precipitation and low temperature heating process. No chemical precursor, surfactant, substrate, template, particle size stabilizer is used for nanoproduct synthesis. Here Cu stripped solution is used as precursor for copper source. Precipitation is achieved with sodium hydroxide. The method of synthesis is explained in section 2.5 of Chapter 2.

In short, metallic clads obtained from separated PCBs (containing 84 wt% copper) were dissolved in 3 M HNO_3 at 30°C for 2 hours, with agitation at 50 g/L pulp density and 500 rpm to yield a solution rich in base metals. Copper was selectively separated from this

solution using liquid-liquid extraction with 30 vol% ACORGA M5640 mixed with kerosene (800 g/L) as the extractant at 20°C, maintaining a pH of 2, a 1:1 organic to aqueous phase ratio, and agitation for 1 hour. Subsequent stripping with 4 M sulfuric acid at pH 0.9 resulted in a purified solution containing 99.9% copper, along with minor amounts of zinc (0.05%) and lead (0.02%). To this strip solution 1 M NaOH solution is continuously added while magnetically stirring the solution until pH of the solution reached 8.5. The solution underwent further magnetic agitation for 1 hour. The resulting mixture was transferred to a Scotch-Durant bottle and sealed tightly. The bottle was placed in an oven at 70°C for 24 hours. Afterward, the supernatant solution was removed, and black-colored precipitates were collected. These precipitates were repeatedly washed with distilled water and methanol using centrifugation to eliminate impurities, then dried overnight at 50°C. This sample was labeled as P1. Another powder sample was prepared similarly, with the Scotch-Durant bottle maintained in the oven at 80°C for 24 hours. This powder was labeled as P2. Schematic of synthesis route is given in *Figure 6.1*.

6.2.1. Analysis of composition of purified strip solution acquired from solvent extraction of leached solution of delaminated WPCBs

The elemental analysis of the Cu-rich starting solution is given in *Table 6.1*. The solution contains a high amount of Cu and negligible amounts of Zn and Pb coming from the spent mobile phone PCBs recycling process.

Table 6.1 Chemical analysis of delaminated metallic fractions during leaching and after solvent extraction purification step.

Element	Delaminated metal fraction (wt%)	Post nitric acid leaching	After solvent extraction and stripping
Cu	83.93	97.39	99.9
Ni	2.34	0.7	-
Zn	0.45	0.49	0.05
Pb	0.1	0.48	0.02
Cd	0.27	0.46	-
Sn	0.45	0.45	-
Fe	0	-	-
Au	0.046	-	-
Ag	0.028	0.001	-
Pd	0.007	0.005	-
Plastic & ceramic residues	12.38	-	-

En dash (-) indicates not detected

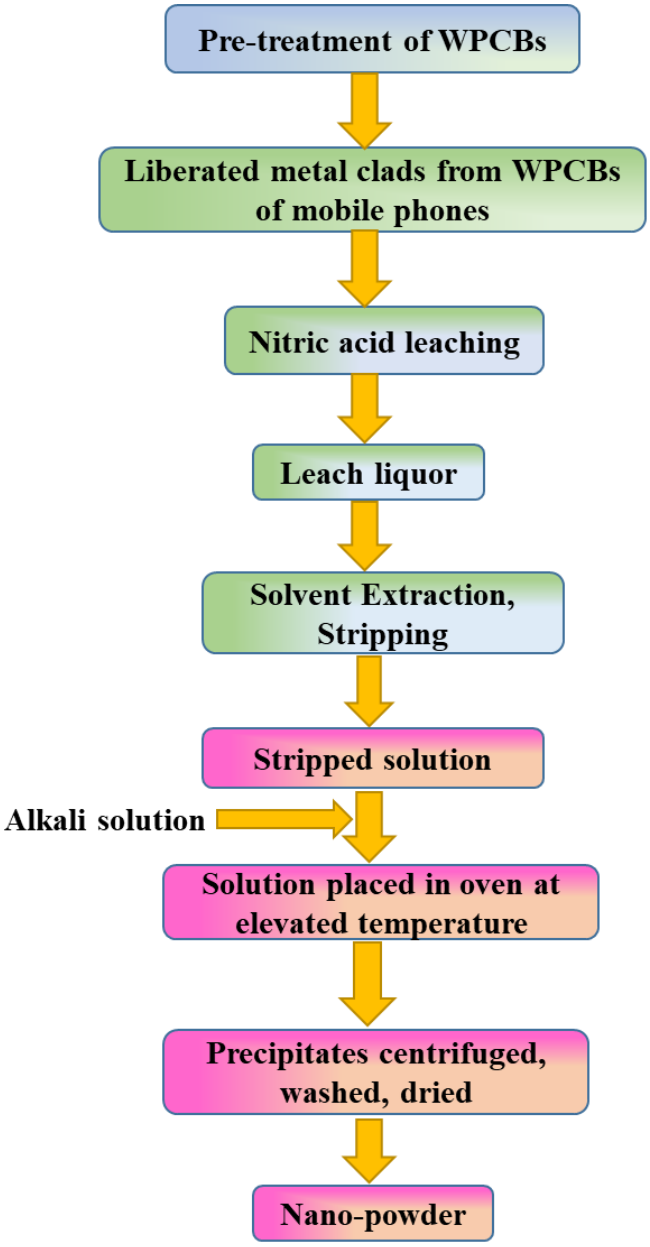

Figure 6.1 Process flowsheet for synthesis of nanoproduct from strip solution of mobile phone PCBs

6.3. Characterization of as-synthesized nanoproduct

6.3.1. Structural properties analysis

To determine the composition of the prepared samples, powder x-ray diffraction was conducted, and the findings are presented in *Figure 6.2*. The peaks of both the samples matched well with base centred monoclinic cupric oxide (JCPDS no. 89-5899). Few low intensity peaks of P1 sample matched with Copper hydroxide (JCPDS no. 13-0420). The pure monoclinic CuO can be identified by two prominent peaks at 2θ=35.5° and 38.6°, associated with the (-111) and (200) crystal planes, respectively. The diffraction pattern did not display any distinctive peaks related to either Cu_2O or Cu, indicating that pure cupric oxide was prepared at 80° C. The formula employed to determine the average crystallite size of the nanostructure is Debye-Scherrer's equation (Parekh et al., 2021). For P1 and P2, the average crystallite sizes were ascertained to be 24.06 nm and 26.08 nm, respectively.

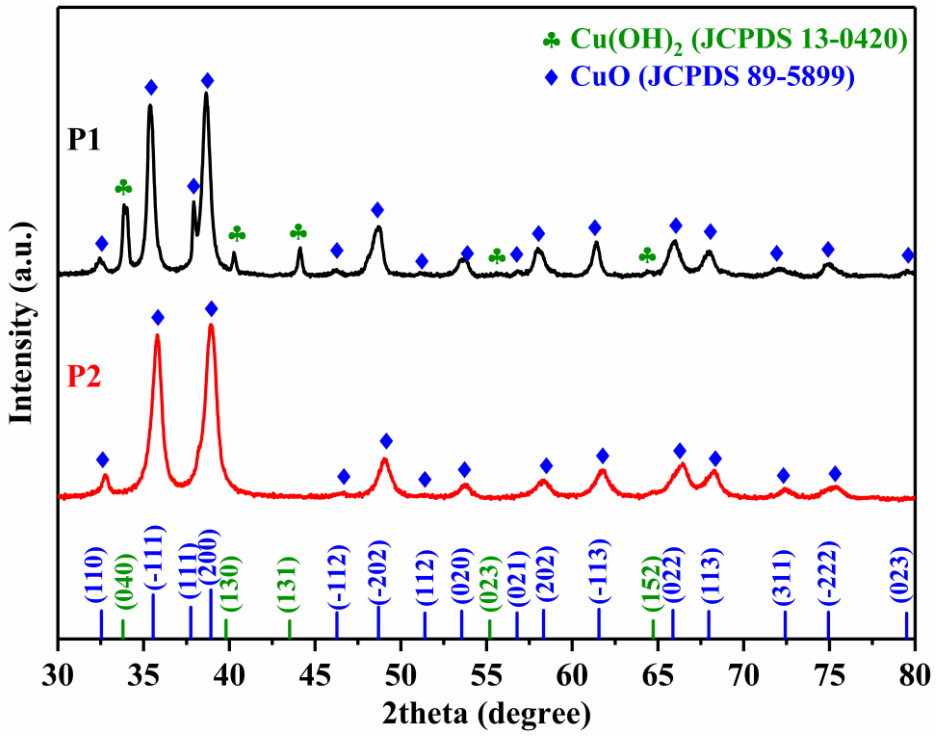

Figure 6.2 XRD analysis of P1 and P2 samples

The FTIR spectra of P1 and P2 are illustrated in *Figure 6.3*. FTIR spectroscopy is a beneficial technique that aids in detecting functional units existing in a molecule. This is achievable by virtue of the distinctive energy absorption band exhibited by each specific chemical bond (Li and Bai, 2005). Absorptions around 3600-3200 cm^{-1} is attributed to the presence of hydrogen-bonded O-H groups. The spread of the band is linked to the degree of hydrogen bonding that occurs with adjoining OH arrays (Henrist et al., 2003). Sharp peak at 1630 cm^{-1} is assigned to the bending mode of hydroxyl group of water (Aguirre et al., 2011). Metal oxide and hydroxide nanoparticles typically exhibit an absorption peak in the characteristic region (wavenumbers below 1000 cm^{-1}) because of vibration between atoms (Chan et al., 2022). Absorption band at 993 cm^{-1} for P1 is ascribed to the bending vibrations of Cu-O-H (Deka et al., 2016). The presence of band at 523, 525, and twin crests at 616, and 636 cm^{-1} is due to bending vibration of the Cu-O bond (Chan et al., 2022; Elwakeel and Guibal, 2015; Rajkumar et al., 2022; Raul et al., 2014; Singh et al., 2016). The stretching of Cu-O along the [-202] direction, caused by the presence of CuO in the monoclinic phase, results in the appearance of peaks within the 600 to 1050 cm^{-1} range (Singh et al., 2016). The absence of impurity peaks corresponding to CH_2, CH_3, or other metal-oxide phases of Zinc or lead phases in the FTIR spectrum confirms the presence of pure CuO.

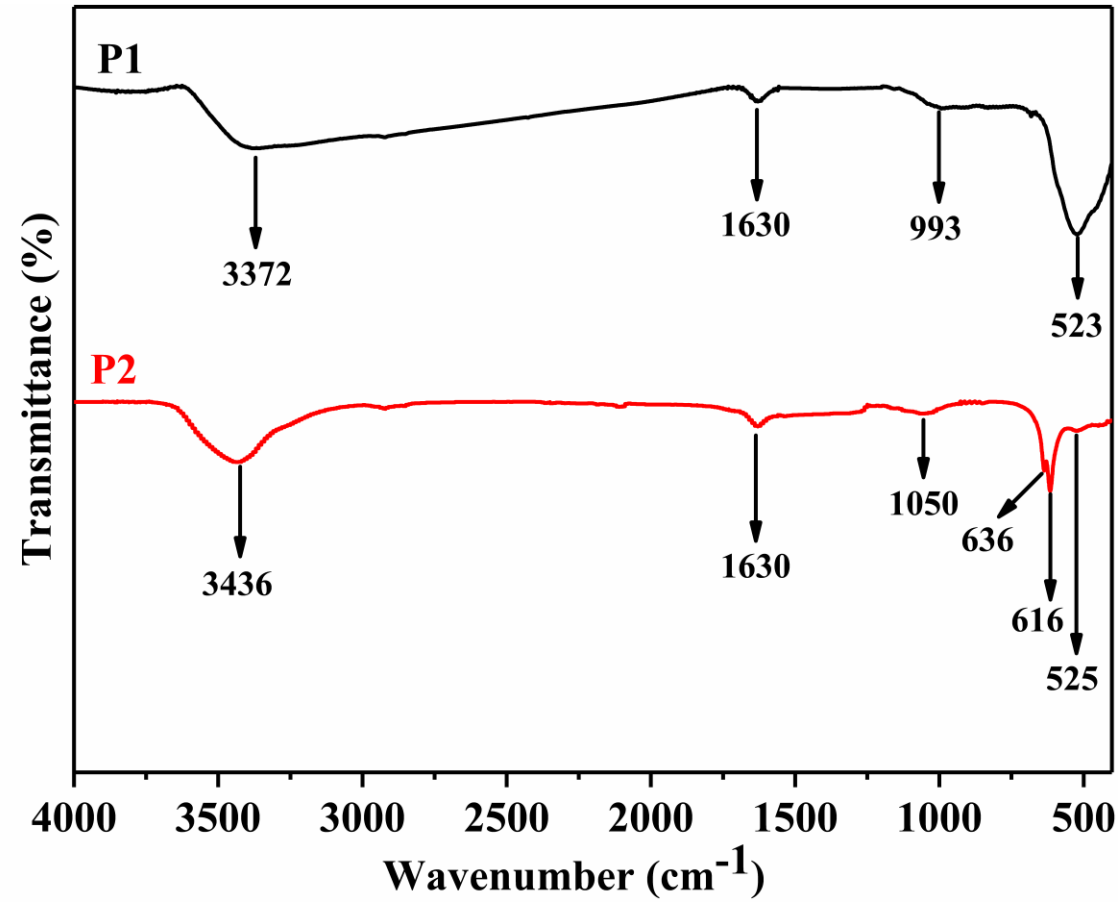

Figure 6.3 FTIR analysis of P1 and P2 samples

Figure 6.4 demonstrates the FESEM-EDX analysis of the P1 and P2 powder samples. *Figure 6.4(a)* shows nanoflakes morphology of as-synthesized P1 sample. *Figure 6.4(c)* shows ridged-spherical morphology of as-synthesized P2 sample. To fathom the morphology of these products and to determine their purity, the EDX of P1 and P2 nanostructures was performed. The obtained EDX spectra of P1 (*Figure 6.4 (b)*) and P2 (*Figure 6.4 (d)*) revealed that elements Copper, Oxygen and Carbon were present. The presence of Carbon tape used to secure the powder sample can account for the observed C peak (Mbenga et al., 2022). Besides, the observed Oxygen peak confirmed that Cu is present in its oxidized form (Adeyemi et al., 2022). Additionally, the absence of any impurity peak observed in both spectra suggested the purity of the prepared nano-product.

Based on the EDX data, it was found that the synthesized CuO had a greater concentration of Copper and a lower concentration of Oxygen. EDX analysis showed that for P1, the weight composition was 81.45% Cu and 18.55% O, while for P2, it was 74.23% Cu and 25.77% O. The atomic ratio of Copper and Oxygen for P1 and P2 were found to be 52.51:47.49 and 42.04:57.96, respectively. These ratios are approximately equal to 1:1, indicating that the product can be identified as CuO.

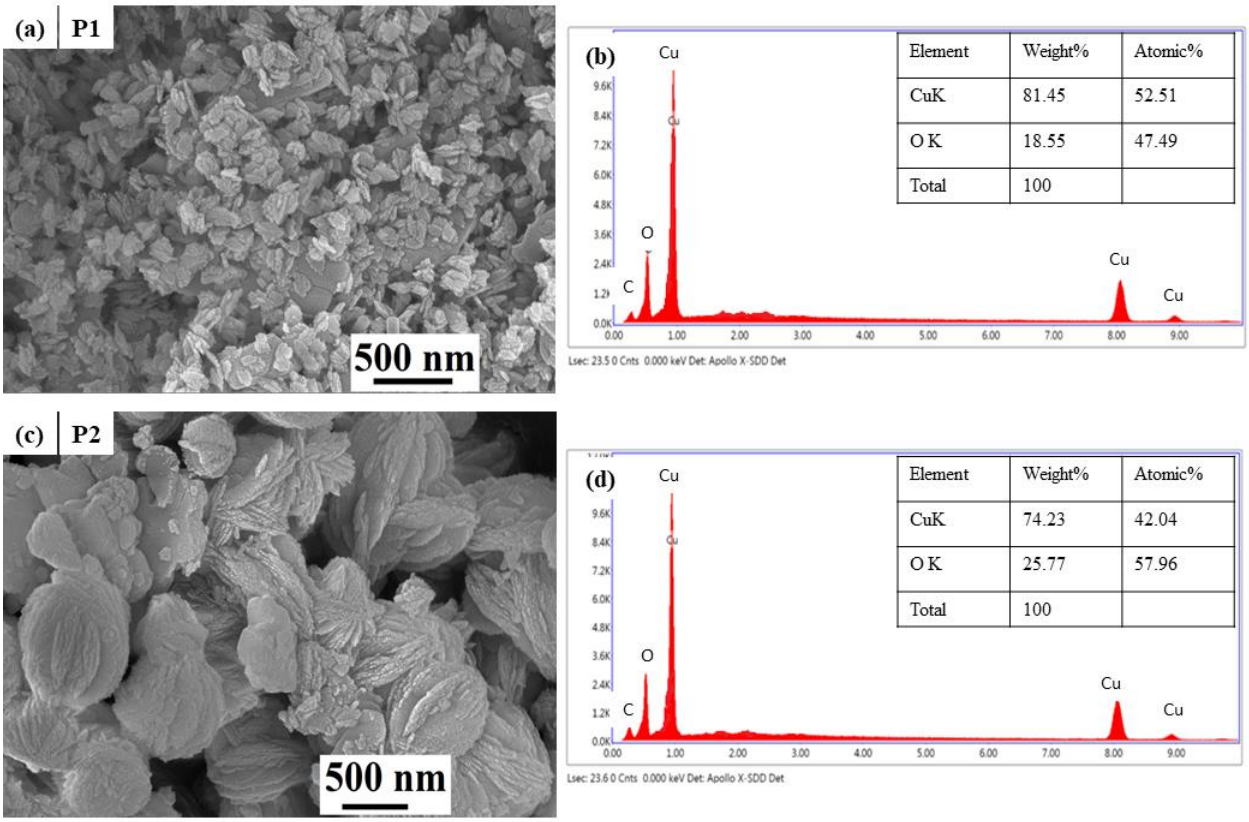

Figure 6.4 FESEM-EDX image of P1 (a,b) and P2 (c,d)

6.3.2. Optical bandgap energy analysis

Solid state UV-visible analysis was done to find the bandwidth energy of as-synthesized P1 and P2 samples using Tauc's formula (Elkodous et al., 2019; Yu and Zhang, 2009):

$$(\alpha h\nu)^n = A(h\nu - E_g) \quad (6.1)$$

In the given *Eq. (6.1),* the symbol α represents the molar absorptivity coefficient, while h connotes Plancks's constant and ν stands for the frequency of light. The letter A represents a material constant, while E_g stands for the bandgap energy of the semiconductor. The symbol n represents the type of transition value, which takes a value of either 2 or ½ depending on whether the semiconductor has transition via a direct or indirect pathway, respectively (Gautam et al., 2023). To determine the value of E_g for a direct pathway transition semiconductor, we draw a straight line on the linear section of the plot of $(\alpha h\nu)^2$ versus hν and extrapolate it until it intersects with the x-axis at α=0. The point of intersection corresponds to the bandgap energy (E_g) for the direct transition semiconductor. By examining the data presented in *Figure 6.5*, we can determine the value of the direct band gap to be 2.28 eV and 2.22 eV for P1 and P2 nanostructure respectively. The raise in the optical band gap energy of CuO NPs is a common effect resulting from quantum confinement, which occurs in nano-sized particles (Liu et al., 2006). As the particle size of CuO increases, the direct band transition energies decrease, as noted in previous research (Rehman et al., 2011).

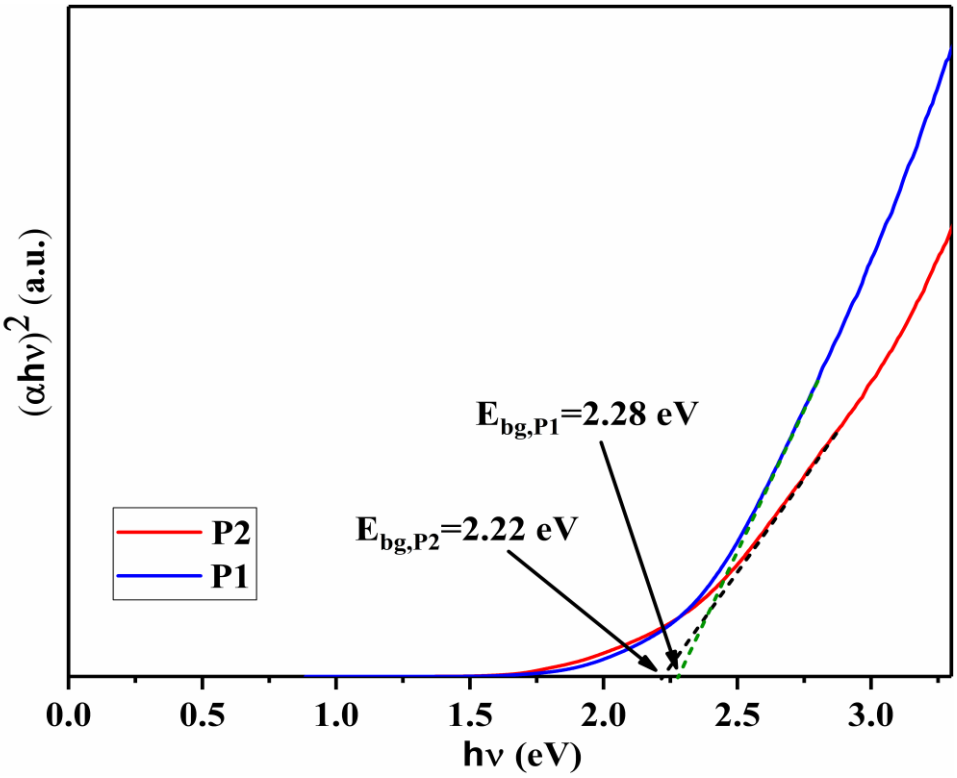

Figure 6.5 Direct bandgap of P1 and P2 found from Tauc's plots

6.3.3. XPS analysis

Figure 6.6 displays the XPS survey spectra for the P1 and P2 samples, calibrated using C 1s at 284.8 eV. The comprehensive spectrum verifies the presence of Cu, O, and C without any evident detection of impurities. The atomic weight percentages of respective elements obtained by XPS spectra are mentioned in *Table 6.2*. *Figure 6.7(a,b)* showcases the high resolution plots depicting the Cu 2p region for sample P1 and P2. The peaks representing Cu $2p_{3/2}$ are positioned at binding energies of 933.6 eV and 933.7 eV, while those corresponding to Cu $2p_{1/2}$ are situated at binding energies of 953.5 eV and 953.4 eV, respectively, for P1 and P2 samples. The primary excitation peaks at approximately 933 and 953 eV represent the distinctive features of Cu^{2+}, while the accompanying shake-up satellite peaks indicate the clear presence of divalent state of an unoccupied $3d^9$ shell, corresponding to the existence of Cu^{2+} i.e. in alignment with CuO (Wang et al., 2018; Yu

et al., 2015). The Cu $2p_{3/2}$ and Cu $2p_{1/2}$ peaks, exhibiting nearly 20.14 and 19.7 eV splitting for P1 and P2 respectively, were associated with the presence of the Cu^{2+} chemical state, indicating the formation of CuO and/or $Cu(OH)_2$ on the samples' surface (Akhavan et al., 2011).

The oxygen state (O 1s) can serve as an anion within the lattice of CuO and Cu_2O, or create the hydroxide group and bond with water molecules when adsorbed onto the material's surface, termed as chemisorbed oxygen (Al-Jawhari and Alhebshi, 2022). So the O 1s was deconvoluted to approximate the different oxygen types present in these nanomaterials. *Figure 6.7(c, d)* show the high resolution O 1s XPS spectra for the P1 and P2 samples. The deconvolution of the O 1s peak reveals distinct sections for chemisorbed oxygen, lattice oxygen, and oxygen vacancy. The oxygen vacancy curves for both P1 and P2 O 1s peaks exhibited significant areas. However, the oxygen vacancy curve area for the P1 sample is notably greater, suggesting a higher presence of oxygen vacancies. Moreover, it's apparent that both samples have surface water molecules, as evidenced by the peak at 533.4 eV. These might have been absorbed from ambient humidity prior to conducting the XPS measurements (Al-Jawhari and Alhebshi, 2022). The O 1s primary excitation at 534 eV in the P1 sample is likely a result of the oxygen, anticipated due to the inclusion of NaOH during the sample's processing (Marathey et al., 2019).

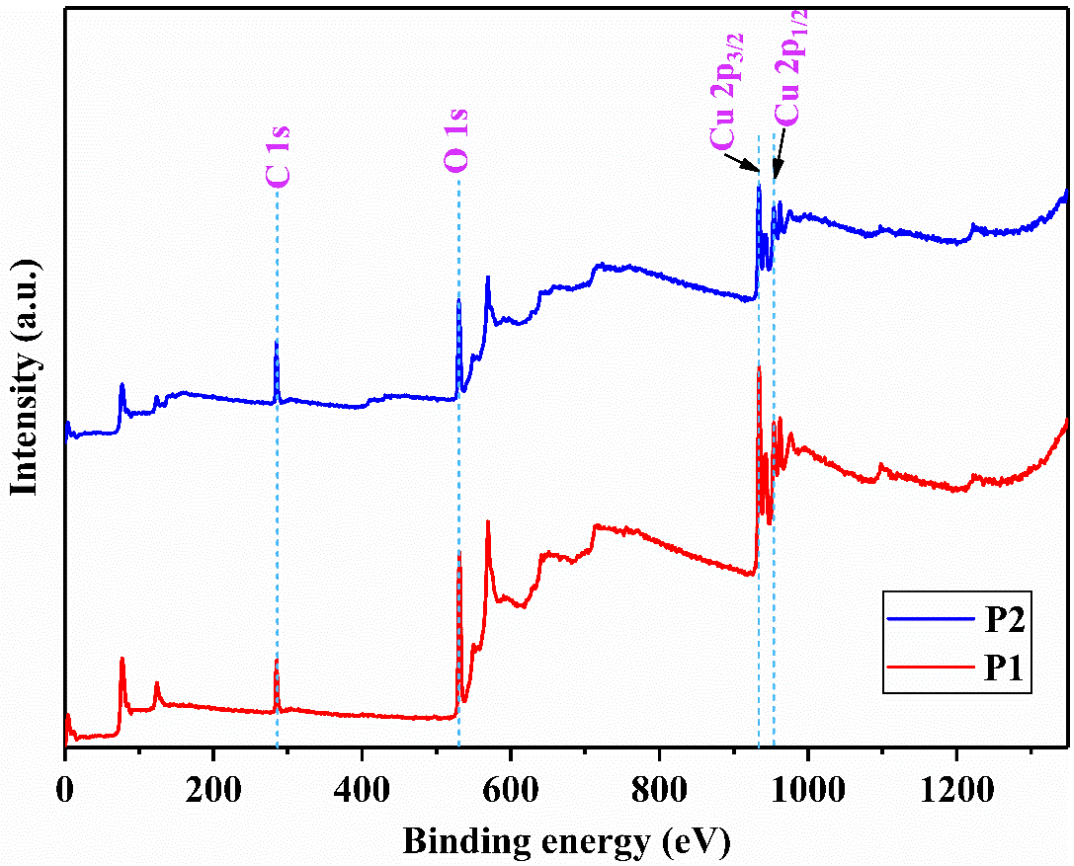

Figure 6.6 XPS spectra for samples P1 and P2

Table 6.2 Atomic weight% of elements present in P1 and P2

Sample name	**Atomic %**		
	Cu 2p	**O 1s**	**C 1s**
P1	21.39	50.01	28.60
P2	15.44	36.44	48.09

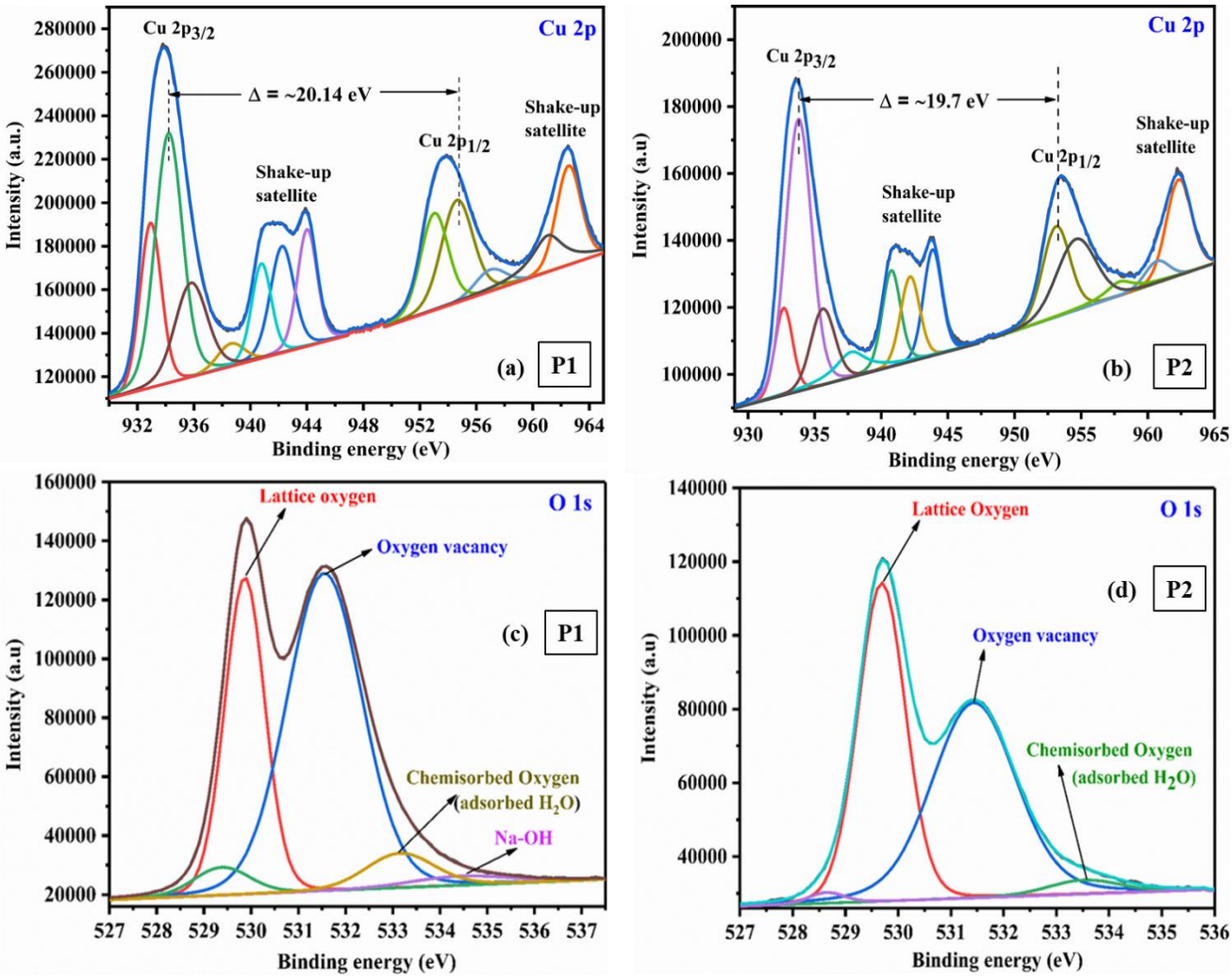

Figure 6.7 High resolution deconvoluted XPS spectra for (a,b) Cu 2p (samples P1 and P2) and (c,d) O1s (samples P1 and P2)

6.3.4. TEM micrograph Analysis

Since the photocatalytic property of P1 nanoproduct is better than P2 (studied in section 6.4), so we did the TEM analysis of P1 as shown in *Figure 6.8* to inspect the detailed morphological structure of the nanostructures. *Figure 6.8(a-c)* presents the representative TEM micrographs at various magnifications. The electron diffraction pattern, known as SAED pattern (*Figure 6.8 (d)*), displays distinctive electron rings that indicate the polycrystalline nature of P1, with discrete spots being visible (Edington, 1975). The

diffraction rings visible in the SAED pattern are in agreement with the XRD analysis. High resolution TEM image of P1 nanoflakes (*Figure 6.8 (e)*) indicates that the interplanar lattice spacing was calculated to be ~0.171 nm, analogous to the distance of (020) plane of CuO crystal in monoclinic form, which is congruous with the XRD datasets. *Figure 6.8(c)* revealed that the ends of the P1 nanoparticles separated into "finger-like" projections. The surface of these nanoflakes is rough and uneven, and they appear to be composed of smaller nanoparticles that have agglomerated together (Wang et al., 2012). The TEM images of P1 reveal that $Cu(OH)_2$/CuO nanoflakes are of flake-like morphology with average width of 22±3 nm. *Figure 6.9* illustrates the size distribution histogram of the $Cu(OH)_2$/CuO nanoflakes.

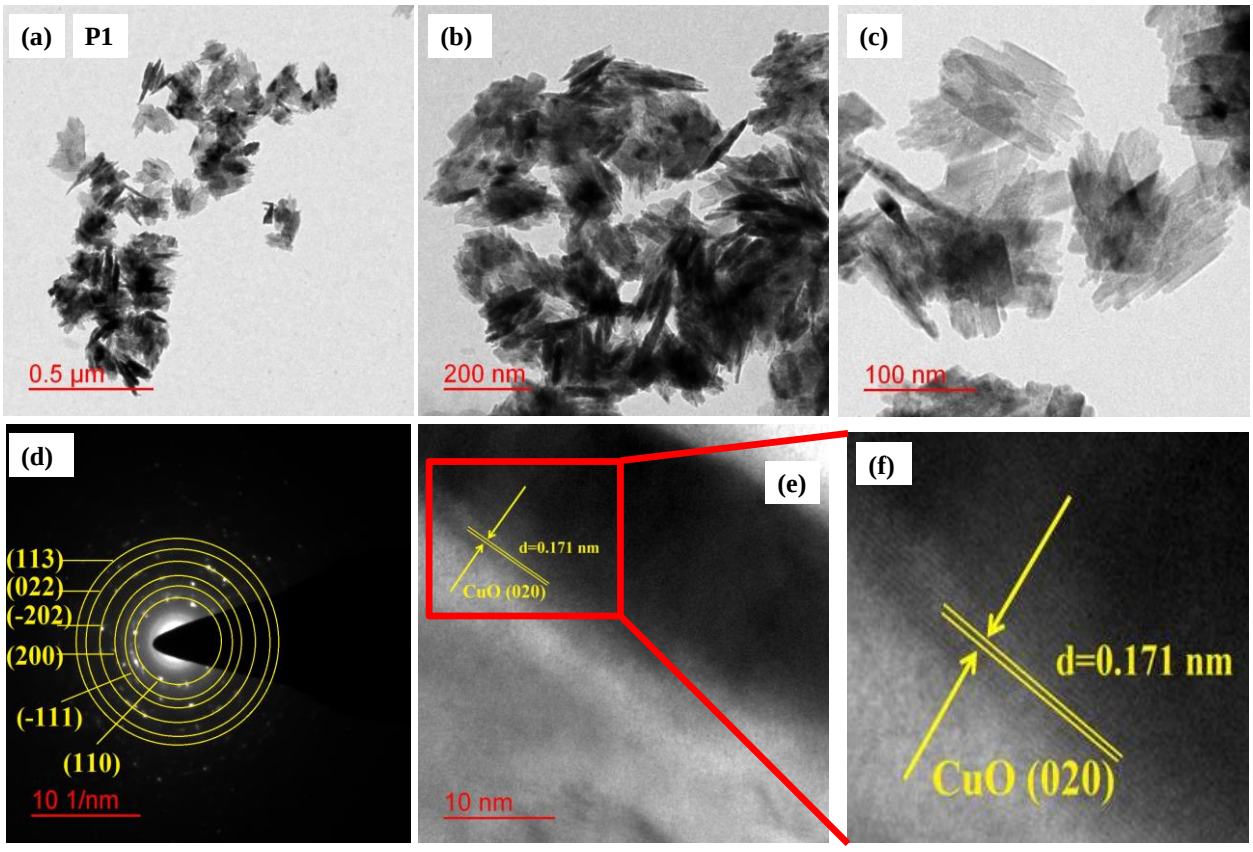

Figure 6.8 TEM micrographs of P1 at varying magnifications (a-c), SAED pattern (d), interplanar spcing in high resolution image (e), zoom-in view of distinct planes (f)

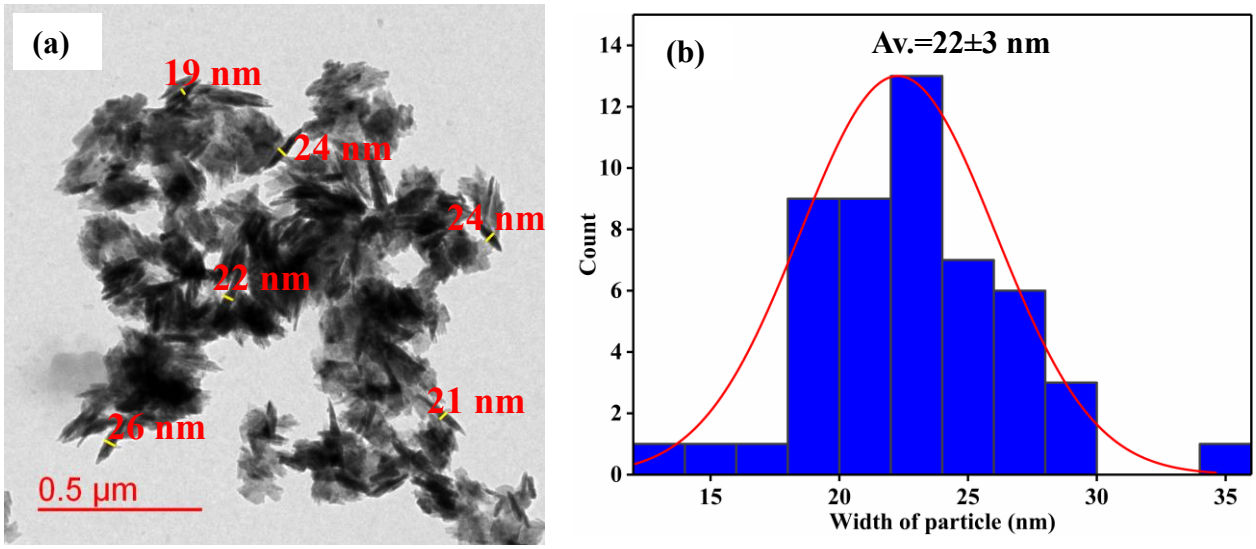

Figure 6.9 Particle width distribution plot

6.4. Photocatalytic activity measurement

With their narrow energy gaps, cuprous oxide (Cu_2O), cupric oxide (CuO), and copper hydroxide ($Cu(OH)_2$) emerge as promising contenders for these reasons (Meyer et al., 2012). Furthermore, photocatalysts comprising heterogenous structures that incorporate two or more copper compounds, such as Cu_xO@Cu (Al-Jawhari et al., 2019; Alhebshi et al., 2020; Sun, 2015) or Cu_xO-$Cu(OH)_2$ (Hu et al., 2020; Murugadoss et al., 2021), have demonstrated higher efficiency compared to pure copper oxides. This improved performance can be attributed to the creation of heterojunctions, which enhance the separation of electron-hole pairs generated during photocatalysis, thereby enhancing the overall photocatalytic activity (Mamba et al., 2017). Marathey et al. reported that hierarchical nanostructure and nanoheterojunctions offer improved performance, such as enhanced charge storage, by facilitating thermodynamically favourable charge transport from multiple active components when compared to the single-phase material (Marathey et al., 2019). Hence heterojunction hybrid nanomaterials are of great importance in photocatalysis as well as energy storage materials.

Rhodamine blue (RhB) is a commonly used coloring agent in dyeing, textile, and food production industries. Chemical structure of RhB is given in *Figure 6.10*. It is also a fluorescent tracer for water (Chandra et al., 2015). However, RhB is carcinogenic in nature even at low concentration, and can cause significant harm to living beings, including irritation of the skin, eye, and respiratory system (Khaki et al., 2017). As a result, there is a constant need to develop a degradation system that can effectively remove organic pollutants and mitigate water pollution issues. Several methods were utilized, including microwave-assisted decomposition (He et al., 2009), adsorption (Waheed et al., 2019), heterogeneous Fenton-like photodegradation (He et al., 2018), LED-assisted catalysis (Natarajan et al., 2011), photodegradation with/without oxidants using various light sources, employing chemical, electrochemical, and photochemical processes (Akram et al., 2020). These techniques have certain downsides such as requirement of costly materials, increased operational expenses, prolonged degradation duration, and incomplete degradation. So we are utilizing the nanomaterial derived from strip solution of PCBs to study the degradation of RhB textile dye in the presence of visible light.

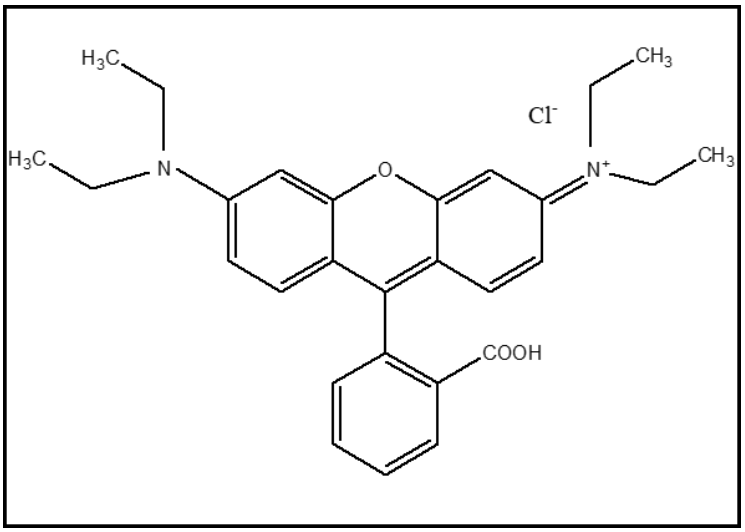

Figure 6.10 Chemical structure of Rhodamine blue

6.4.1. RhB degradation

To evaluate the photocatalytic performance of P1 and P2 samples, their ability to degrade RhB under visible light was studied. A mixture comprising 2 ml of distilled water, 200 µl of a RhB solution in water (4 ppm), and 50 µl of a dispersed nanoparticle solution was placed in a 4 ml cuvette. The nanoparticle dispersion solution was created by adding 2.1 mg of solid catalyst to 3 ml of distilled water. The solution was initially stirred in darkness for 15 minutes to achieve full equilibrium, followed by exposure to light for a specific trial duration. Four Philips LED bulbs served as the visible light source in the chamber. The degradation of RhB was monitored at defined intervals using a UV-visible spectrophotometer.

The P1 and P2 samples that were synthesized were able to achieve the degradation of RhB through visible light illumination. *Figure 6.11(a-c)* shows the UV-visible absorbance spectra of the disintegration of RhB dye measured at various time periods. RhB demonstrates visible light absorption, most prominent at a wavelength range of 542 to 554 nm (Haseena et al., 2019). Under visible light irradiation, the primary peak of absorption of the RhB dye solution was noted to gradually diminish in the presence of the photocatalyst. *Figure 6.11(a)* shows that RhB did not exhibit any degradation without catalysts (P1 or P2). The degradation of RhB occurred only when a photocatalyst was present in the reaction mixture (as shown in *Figure 6.11(b,c)*). The removal efficiency of the dye initially increases for P2 which has large particle size, but then it starts to decrease once the particle size surpasses a certain threshold, whereas the removal efficiency keeps on increasing for P1 which has smaller particle size than P2. This phenomenon can be attributed to the behaviour of the adsorbent particles when their particle size exceeds a certain value, the accessibility of the dye to the adsorbent pores declines, resulting in a

subsequent decrease in efficiency (Elshabrawy et al., 2023). The percentage of RhB degradation was determined using equation

$$\% \text{ Degradation} = \left(\frac{C_0 - C}{C_0}\right) \text{x } 100 \quad (6.2)$$

In the given *Eq. (6.2)*, C_0 represents the starting concentration of dye, while C denotes the concentration of dye at time t after subjecting to visible radiation. *Figure 6.11(d)* shows that RhB exhibited a degradation of 97.28% with P1 ($Cu(OH)_2$/CuO) and 14.64% with P2 (CuO) at 100 minutes time period. *Figure 6.11(e)* depicts the graphs for experiments conducted in the presence and absence of a catalyst (blank). The data regarding the degradation of RhB was analyzed using zeroth, first, and second order kinetics to determine the appropriate model for the reaction. The most suitable fitting for the data was achieved with the first-order kinetics model. *Figure 6.11(f)* shows the variation of $-\ln(C/C_0)$ with radiation time in accordance with the *Eq. (6.3)* provided below

$$-\ln(C/C_0) = k_{app}t \quad (6.3)$$

In this context, C represents the concentration of RhB at a given time t, while C_0 is the starting concentration of RhB. The symbol k_{app} denotes the apparent rate constant. From the linear fitting, the rate constants for the sample with the catalyst P1, P2, and without the catalyst were determined to be 0.00397 min^{-1}, 0.00101 min^{-1}, and 0 min^{-1}, respectively.

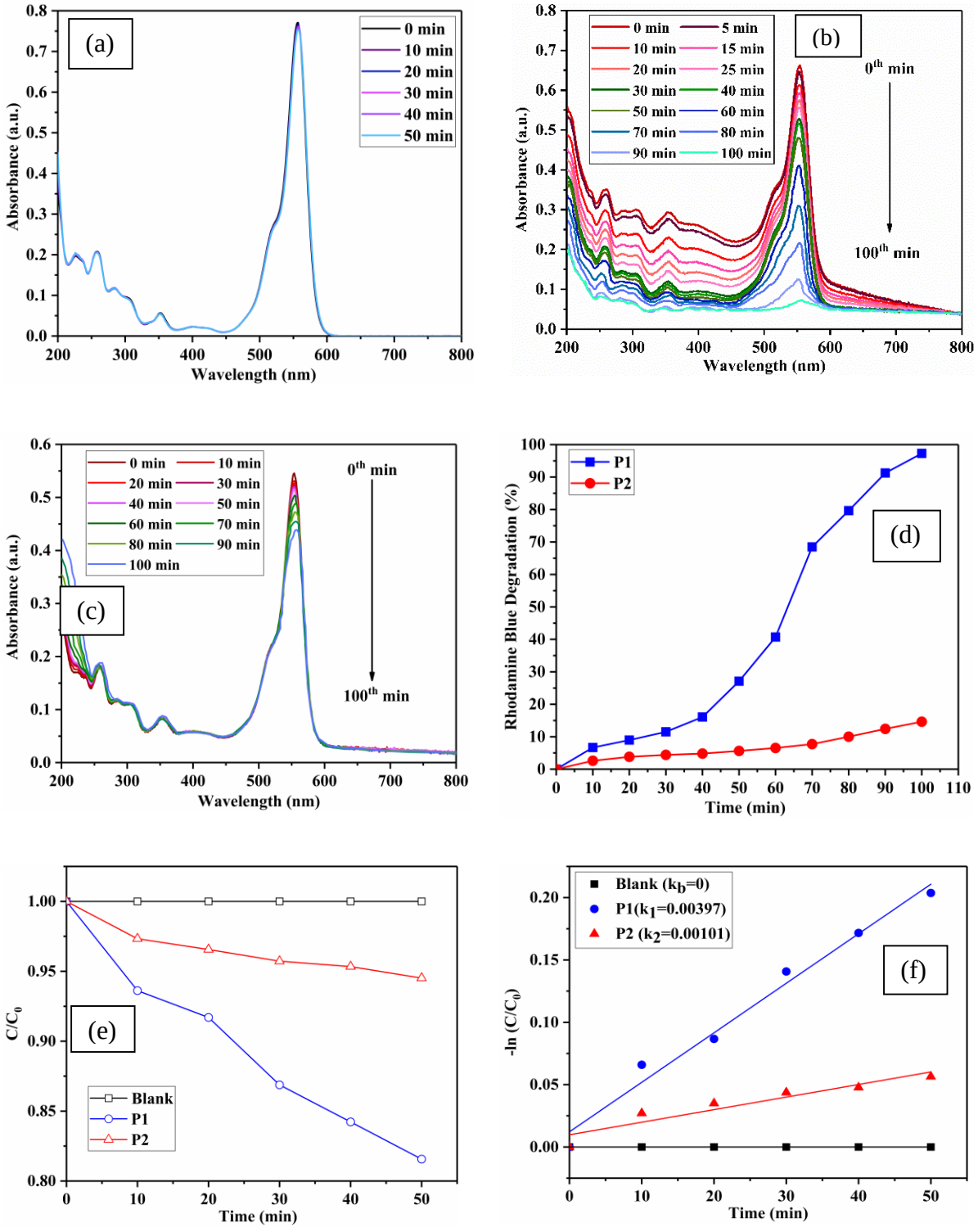

Figure 6.11 UV-visible spectra of RhB degradation without catalyst (a), with P1 (b) and P2 (c) at different time intervals under visible light, (d) percentage degradation of RhB upon reacting with P1 and P2, and its Kinetic study (e,f)

The comparative evaluation of RhB degradation using $Cu(OH)_2$/CuO and CuO photocatalyst, as documented in various literatures (AlSalhi et al., 2019; Dodoo-Arhin et al., 2021; Haseena et al., 2019; Leong et al., 2022; Phutanon et al., 2018; Sanjini et al., 2017; Truong et al., 2022; Yaseen et al., 2022; Zeng et al., 2018), is presented in *Table 6.3*.

Table 6.3 A comparison of the reported efficiency of RhB degradation using photocatalysts in various light sources

Photocatalyst	Synthesis method	Particle size	Bandgap energy (eV)	Model Pollutant concn	Illumination source	Degradation (%)	Time of reaction (min)	References
Porous CuO nanofibers	Precipitation followed by oxidation	80-150 nm	1.78	10 mg/L	Visible light+H_2O_2	96	160	Zeng et al., 2018
Achyranthes aspera-treated CuO	Reducing agent assisted co-precipitation method	15 nm	2.5	10 mg/L	Visible light	91	180	Haseena et al., 2019
Crotalaria verrucosa-treated CuO			2.32			96	180	
CuO/ZnO nanoparticles	Precipitation	-	2.12	10 ppm	Visible light	96.63	150	AlSalhi et al., 2019
CuO flower	Self-assembly	100 nm	-	1 ppm	Visible light	85	240	Phutanon et al. 2018
CuO nanoparticles	Microwave assisted precipitation	30-60 nm	2.8	10 mg/L	UV light	100	210	Sanjini et al., 2017
ZnO/CuO nanoparticles	Sol-gel method	30 nm	3.05	10 ppm	Sunlight	98	180	Truong et al.,2022
CuO-doped TiO_2	Sonochemical method	120-240 nm	2.94	15 ppm	Visible light	65	360	Leong et al., 2022
CuO	Solution precipitation	-	2.4	50 mg/L	Visible light	99.6	100	Dodoo-Arhin et al., 2021
CuO-SiO_2 composite	Sol-gel process	-	3.419	-	Visible light	85	300	Yaseen et al., 2022
$Cu(OH)_2$/CuO nanoflakes (P1)	Precipitation	22±3 nm	2.28	40 mg/L	Visible light	97.28	100	This Study

En dash (-) indicates data unavailable

6.4.2. Plausible photocatalytic mechanism

A possible photocatalytic mechanism for RhB degradation is illustrated in the schematic diagram shown in *Figure 6.12***.** Exposure of a photocatalyst to visible light results in the creation of pairs of electrons and holes. During this process, free electrons move from the valence band to the conduction band, leaving behind a hole in the valence band (Chen and Ray, 1998). The number of electron-hole pairs generated is contingent on both the strength of the light and the material's electronic properties. As long as the charge separation persists in a photocatalytic procedure, both electrons and holes will shift towards the surface of the catalyst. There, they have the opportunity to partake in redox reactions and interact with species adsorbed on the surface. When holes are present in the valence band, they can interact with surface-bound H_2O or OH^- to form reactive species like hydroxyl radical ($O_2^{\cdot -}$), which can be used to break down dye molecules. It is assumed that the degradation of RhB dye molecules through photocatalysis involved the use of highly reactive $O_2^{\cdot -}$ and $OH^{\cdot}$ species (Azimi and Nezamzadeh-Ejhieh, 2015; Subash et al., 2014; Wu et al., 2010). Nonetheless, without electron-hole scavengers, the electron-hole pairs produced by light absorption may combine again in a matter of nanoseconds, resulting in the dissipation of input energy as heat. Hence, electron accepting species are crucial for an effective photocatalytic process.

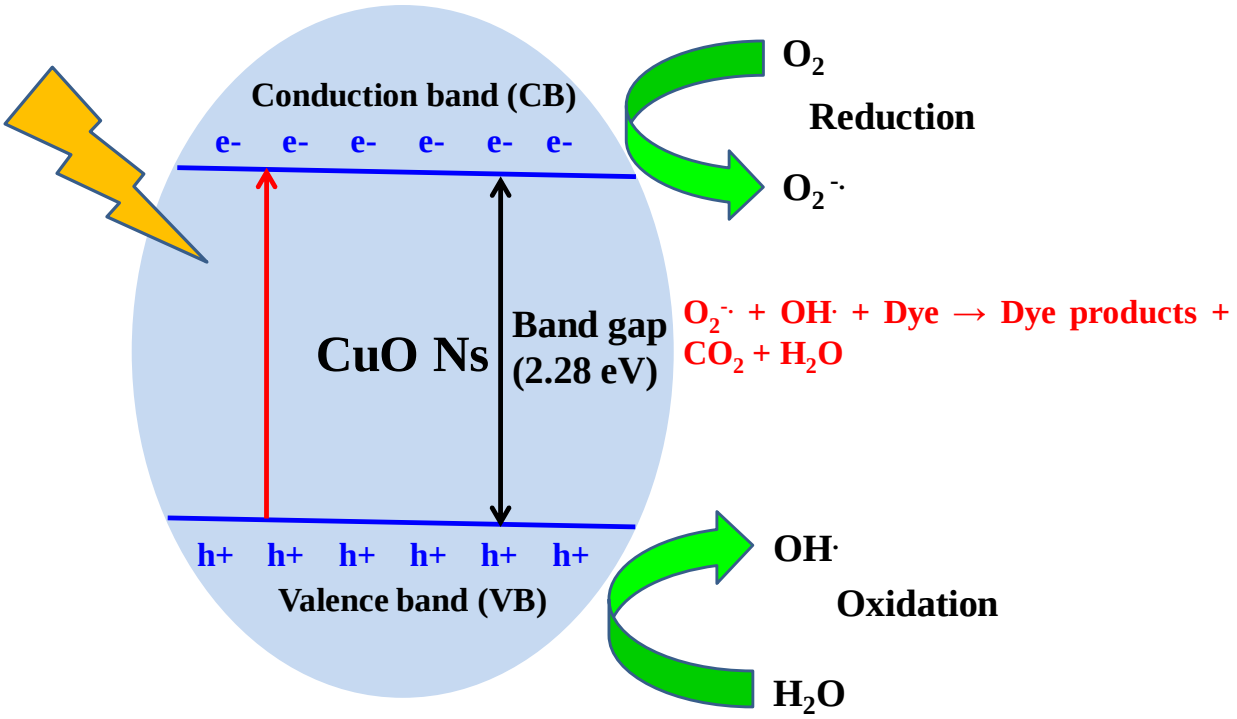

Figure 6.12 A diagrammatic illustration of the possible photocatalytic mechanism

6.4.3. Understanding the photocatalytic behaviour of P1 and P2

Studies have indicated that photocatalytic behaviour strongly correlates with factors such as particle size, surface area, particle size distribution, and bandgap. P1 ($Cu(OH)_2$/CuO) exhibited better photocatalytic behaviour than P2 (CuO). This can be contributed to following reasons:

i. As evident from the FESEM morphology image and size distribution plot drawn from TEM micrographs, it is clear that the particle size of P1 (i.e.22±301 nm) is less than that of P2 (i.e. 785.975±5.402). Due to small particle size of P1 and irregular nanoflake morphology, the surface area available for dye degradation reaction is more for P1 than for P2. Higher surface area offers transmission paths for organic dye molecules, which can sufficiently access the photocatalytic active

sites of the photocatalyst, hence increasing the reactivity and adsorption of dye (Marathey et al., 2019).

ii. Structure with lower average crystallite size shows better photocatalytic property than that with higher average crystallite size (Marathey et al., 2019). As calculated in XRD analysis, P1 has lower crystallite size (i.e. 21.06 nm) than P2 (i.e. 26.08 nm).

iii. As found from the deconvoluted O 1s XPS peaks, it is evident that P1 contains more oxygen defects or oxygen vacancies than P2. Oxygen vacancy percentage for P1 is 52.91% and for P2 is 43.07%. Oxygen vacancies act as electron-hole acceptors during the photocatalytic reaction, thus reducing the recombination rate which is necessary for an enhanced photocatalysis process. Oxygen vacancies also facilitate the adsorbed oxygen to capture photoinduced electrons, synchronously generating superoxide radical anions, thereby enhancing the photocatalytic property (Marathey et al., 2019).

iv. In P1, the –OH of $Cu(OH)_2$ serve as electron acceptors for the photogenerated holes, leading to the formation of hydroxyl radicals ($-OH^{\cdot}$) and preventing the reincorporation of electron-hole pairs in the $Cu(OH)_2$/CuO photocatalyst, as stated in former studies (Akhavan et al., 2011; Wang et al., 2015). The photoexcited hole in the photocatalyst $Cu(OH)_2$/CuO interacts with the surface –OH bonds of $Cu(OH)_2$ to generate $OH^{\cdot}$ radicals. This process can be considered as a significant factor in degradation, as $OH^{\cdot}$ radicals are an essential parameter in this process.

v. Another reason for the high activity of $Cu(OH)_2$/CuO (P1) photocatalyst can be assigned to the interface between $Cu(OH)_2$ and CuO. This interface contains higher

valence sites of Cu(II) in the hydroxide layer, which may facilitate the capture of photogenerated electrons (Wang et al., 2015). This results in the creation of surplus superoxides and/or hydroxyl radicals on the photocatalyst surface, which adds to superior photocatalytic performance of $Cu(OH)_2$/CuO photocatalyst (Saratale et al., 2018).

Congo red and methylene blue were not used in this study (chapter 6) in the presence of P1 and P2 nanoproducts as P1 and P2 showed lesser CR and MB degradation compared to N1, N2, N3, and N4, whereas P1 and P2 showed better photocatalytic degradation of RhB compared to N1, N2, N3 and N4. The photocatalytic activity of different photocatalysts varies with the differences in the lattice mismatch, BET surface area, impurities on the catalyst's surface, particle size, morphology, surface properties of catalyst, shape of particles, type of model pollutant (here, dye), initial concentration of dye and catalyst, source and intensity of light etc. (Dursun et al., 2020; Reza et al., 2017). It is well known that metal oxides grown by chemical bath method have excess oxygen vacancies in their grown structures (Zaman, 2012; Zaman et al., 2012). The P1 (52.91%) grown by this method contains excess oxygen vacancies compared to N1 (35.88%), and P2 (43.07%). Water dissociates on oxygen vacancies. The water adsorbs dissociatively in oxygen vacancies and via proton transfer to a neighboring bridging oxygen atom creating two bridging hydroxyl groups per initial vacancy. So we expect that the oxygen vacancies act as active sites for water dissociation on CuO nanostructures. The reason for the large reactivity of the vacancies is associated with the high energy of the defects. $Cu(OH)_2$/CuO petals contain more oxygen vacancies in their structure and produces more hydroxyl ions which are one of the active species to degrade CR, MB and RhB dyes. Besides, it is reported that the degradation of RhB is higher and more efficient in the presence of CuO petals than

in the presence of CuO flowers (Zaman et al., 2012). So RhB degradation is higher in the presence of P1 than in the presence of N1, N2, and P2 nanostructures.

6.5. Conclusions

In this chapter nanostructures were prepared from strip solution of mobile phone PCBs using precipitation and low temperature ageing method. Moreover, its potential application as a photocatalyst was investigated by degrading RhB in the presence of visible light. The important points relevant to this chapter are given below:

- This study effectively produced CuO and $Cu(OH)_2$/CuO nanostructures by a facile solution technique at low temperature using strip solution obtained from discarded mobile phone PCBs as copper source and sodium hydroxide.
- XRD and FTIR confirmed the generation of $Cu(OH)_2$/CuO and CuO nanocrystallites with average crystallite size of 24.06 nm and 26.08 nm at ageing temperature of 70 and 80°C respectively.
- FESEM showed that at 70°C $Cu(OH)_2$/CuO nanoflakes and at 80°C CuO ridged nanospheres were formed. EDX attached to FESEM established that copper and oxygen were present in the nanostructure, confirming the evolution of CuO.
- The average particle width of the $Cu(OH)_2$/CuO nanoflakes as evaluated from the particle size distribution curve is found to 22±3 nm.
- The bandgap energy calculated from Tauc's plot showed that the nanostructures have bandgap energy higher than their bulk materials.
- $Cu(OH)_2$/CuO nanostructure shows higher oxygen vacancy than the CuO microspheres.

- The as-synthesized nanostructures were assessed of their photocatalytic activity by verifying RhB degradation. $Cu(OH)_2$/CuO nanoflakes exhibited 97.28% RhB degradation under visible light illumination.

- The method presented can be seen as a novel and environment-friendly approach for extracting Copper as $Cu(OH)_2$/CuO hybrid nanomaterial and CuO nanoparticles that can serve as a highly effective photocatalyst for treating wastewater from textile industries.